



PAPER

The biomechanics of simple steatosis and steatohepatitis

RECEIVED
7 February 2018

REVISED
23 April 2018

ACCEPTED FOR PUBLICATION
27 April 2018

PUBLISHED
17 May 2018

K J Parker¹, J Ormachea¹, M G Drage², H Kim³ and Z Hah⁴

¹ Department of Electrical and Computer Engineering, University of Rochester, Hopeman Building, Box 270126, Rochester, NY 14627, United States of America

² Department of Pathology and Laboratory Medicine, University of Rochester Medical Center, 601 Elmwood Ave, Box 626, Rochester, NY 14642, United States of America

³ Department of Biomedical Engineering, University of Rochester, Goergen Building, Box 270168, Rochester, NY 14627, United States of America

⁴ Samsung Medison Co. Ltd, Seoul, Republic of Korea

E-mail: kevin.parker@rochester.edu

Keywords: shear waves, liver, steatosis, ultrasound, MRI, steatohepatitis, elastography

Abstract

Magnetic resonance and ultrasound elastography techniques are now important tools for staging high-grade fibrosis in patients with chronic liver disease. However, uncertainty remains about the effects of simple accumulation of fat (steatosis) and inflammation (steatohepatitis) on the parameters that can be measured using different elastographic techniques. To address this, we examine the rheological models that are capable of capturing the dominant viscoelastic behaviors associated with fat and inflammation in the liver, and quantify the resulting changes in shear wave speed and viscoelastic parameters. Theoretical results are shown to match measurements in phantoms and animal studies reported in the literature. These results are useful for better design of elastographic studies of fatty liver disease and steatohepatitis, potentially leading to improved diagnosis of these conditions.

1. Introduction

One of the major successes of elastography is the demonstrated ability to characterize high grade liver fibrosis by elevated shear wave speed estimates (Cosgrove *et al* 2013, Srinivasa Babu *et al* 2016). What remains unclear are the biomechanics of earlier stages of the progression of liver disease. Specifically, the effect of simple steatosis and inflammation on the shear wave speed measurements, and the changes in rheology as compared with the normal liver are not well understood. Human liver elastographic studies that include assessment of steatosis grades have produced mixed results, likely due to the range of techniques and co-factors present (Barr *et al* 2015, Barr 2018). These conditions are important to understand and characterize since detection of early stages of liver disease creates the opportunity for early interventions and therapies to slow or reverse the pathological changes. Accordingly, in this paper we consider biomechanical or rheological models that can capture the essential changes in the shear modulus of tissues as fat and inflammation increase in a liver from the initial normal state. The structure and composition of the liver tissue determine these changes. To illustrate the effects, figure 1 shows pathology slides from normal, steatotic, and steatohepatitis human livers.

The hepatic architecture changes as macrovesicles of fat (triglycerides) accumulate. If inflammation responses are also prevalent, some cellular swelling and inflammatory foci are present as well. We seek the simplest accurate rheological descriptions that can capture these changes and their effect on shear wave speed. Accordingly, figure 2 provides a schematic and conceptual overview of the proposed models.

In the following sections, we quantify the effects through use of appropriate rheological models. Then experimental results from an oil-in-gelatin phantom are compared with the composite model of spherical inclusions. Finally, other results from well-characterized animal studies are compared with theoretical predictions.

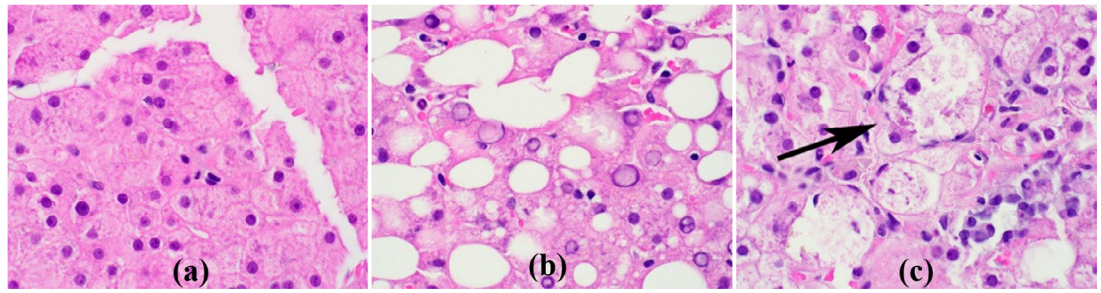


Figure 1. Comparative histology of human liver. (a) Normal liver. Liver parenchyma with normal lobular architecture, and an absence of steatosis and fibrosis. (b) Steatosis. Hepatocytes with pathologic macrovesicular steatosis, forming large intracytoplasmic lipid vacuoles, but without features of steatohepatitis. (c) Steatohepatitis. Macrovesicular steatosis with features of toxic/metabolic injury, including ballooning degeneration (black arrow), and lobular inflammation. H&E stain, 600 \times magnification.

2. Theory

2.1. Spherical particulate inclusions

The theory of the biomechanics of a composite material with spherical inclusions was treated comprehensively in a landmark paper by Christensen (1969). He applied a principle of minimum strain energy in a deformed elastic medium with specifically spherical inclusions. Simplifications for the effective shear modulus were found for the limiting case of the volume fraction of spheres being small or large, the asymptotic approach to volume fraction of zero or one. A more recent overview of different types of composites, inclusion shapes, and results are given in Chapter 9 of Lakes (2009). Here we take the most relevant solution, the low concentration case for small volume fraction V_2 of fat (triglyceride-filled spherical vacuoles) with shear modulus $G_2(\omega)$, in liver where the normal liver is modeled as $G_1(\omega)$ according to a general power law, consistent with many observations over time (Zhang et al 2007, Parker 2015, Ormachea et al 2016). Given $G_2(\omega)$, $G_1(\omega)$, and V_2 , the new composite liver representing simple steatosis will have a shear modulus $G_c(\omega)$ given by:

$$\frac{G_c}{G_1} = 1 - \frac{15(1-\nu_1)\left(1 - \frac{G_2}{G_1}\right)V_2}{7 - 5\nu_1 + 2(4 - 5\nu_1)\frac{G_2}{G_1}}. \quad (1)$$

Assuming the Poisson's ratio $\nu_1 \approx 0.5$, the incompressible limit, and writing the frequency dependence explicitly:

$$G_c(\omega) = G_1(\omega) - \frac{\frac{15}{2}[G_1(\omega) - G_2(\omega)]V_2}{\frac{9}{2} + 3\left[\frac{G_2(\omega)}{G_1(\omega)}\right]}. \quad (2)$$

Let us assume a generalized power law behavior for normal liver, consistent with the Kelvin–Voigt fractional derivative model with E_0 near zero (Zhang et al 2007) and also consistent with the two-parameter microchannel flow model (Parker 2014, 2015). Thus, for normal liver and phantoms, we set

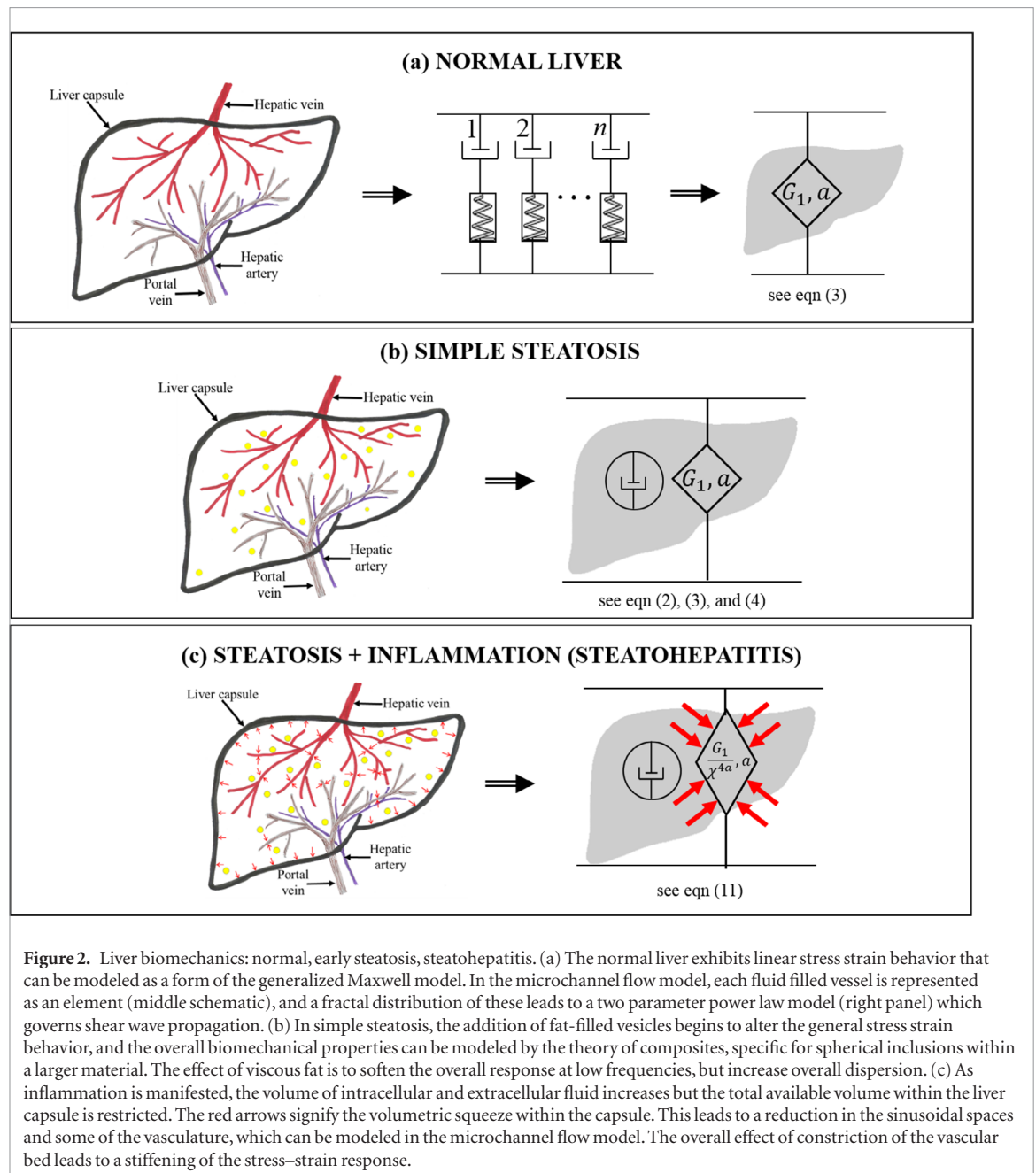
$$G_1(\omega) = G_0(j\omega)^a = G_0 \cdot \omega^a \left[\cos\left(\frac{a\pi}{2}\right) + j\sin\left(\frac{a\pi}{2}\right) \right], \quad (3)$$

where G_0 is a constant, j is the imaginary number, and a is the power law parameter. Initially, we set $G_0 = 4$ kPa and $a = 0.025$; we shall later see these values pertain to our gelatin phantom. Further assume a purely viscous fluid model for the fat within the spherical vacuoles:

$$G_2(\omega) = \eta \cdot j\omega, \quad (4)$$

where $\eta = 0.11$ Pa \cdot s. In that case, the composite has a dramatic change in frequency response of $|G_c(\omega)|$ as shown in figure 3 for a $V_2 = 20\%$ mixture. The striking lesson is that the steatotic composite could be deemed 'softer' (below 70 Hz) or 'harder' (above 80 Hz) or 'no change' (near 75 Hz) depending on what frequency band was employed in different laboratories. The crossover frequency depends on the particular values of $G_1(\omega)$ and $G_2(\omega)$. Thus, for livers with higher $G_1(\omega)$ than the gelatin values (4 kPa) used in figure 3, the crossover frequency will shift higher. Once the $G_c(\omega)$ is specified, the storage modulus and loss modulus can be plotted from the real and imaginary parts of $G_c(\omega)$, respectively. In addition, the complex wavenumber \hat{k} is specified (Blackstock 2000, Carstensen and Parker 2014) as:

$$\hat{k} = \frac{\omega}{\sqrt{\frac{G_c(\omega)}{\rho}}} = \beta - j\alpha = \frac{\omega}{c_p} - j\alpha, \quad (5)$$



where c_p is the phase velocity and α is the attenuation. These can be derived from the real and imaginary parts of equation (5), and are dependent on shear wave frequency and oil percentage, as shown in figures 4 and 5.

2.2. Inflammation and the crowded space

As inflammation progresses, increasing amounts of intracellular and extracellular fluid are associated with the ballooning hepatocytes and other morphological changes shown in figure 1(c). This, in addition to the fat vacuoles, crowds out the available volume within the liver capsule; the effect is schematically represented by the small red arrows in figure 2(c). This in turn leads to reduced volume of sinusoidal spaces, and drop in flow (Wada *et al* 1974, Watson 1991, Selzner and Clavien 2001, Hessheimer *et al* 2009). Over the long term, the capsule can expand, ultimately leading to hepatomegaly (Watson 1991). In the short term, we postulate that the crowding effects reduce the dimensions of the sinusoidal spaces and small vasculature and fluid spaces. This can be modeled in the microchannel flow model to predict changes in shear modulus and shear wave speed. Some examples of changes in vasculature creating changes in shear wave speed have been given in Parker *et al* (2016) and Parker (2017a). Here, we examine the specific cases of the liver under volumetric crowding.

Consider a baseline or resting state with a power law distribution of hepatic vessels and fluid spaces shown in figure 2(a). Under the microchannel flow model (Parker 2014), the fractal branching vasculature is treated as a generalized Maxwell model: each vessel of radius r_n linked to a time constant τ_n by Poiseuille's Law, $\tau_n = C/r_n^4$,

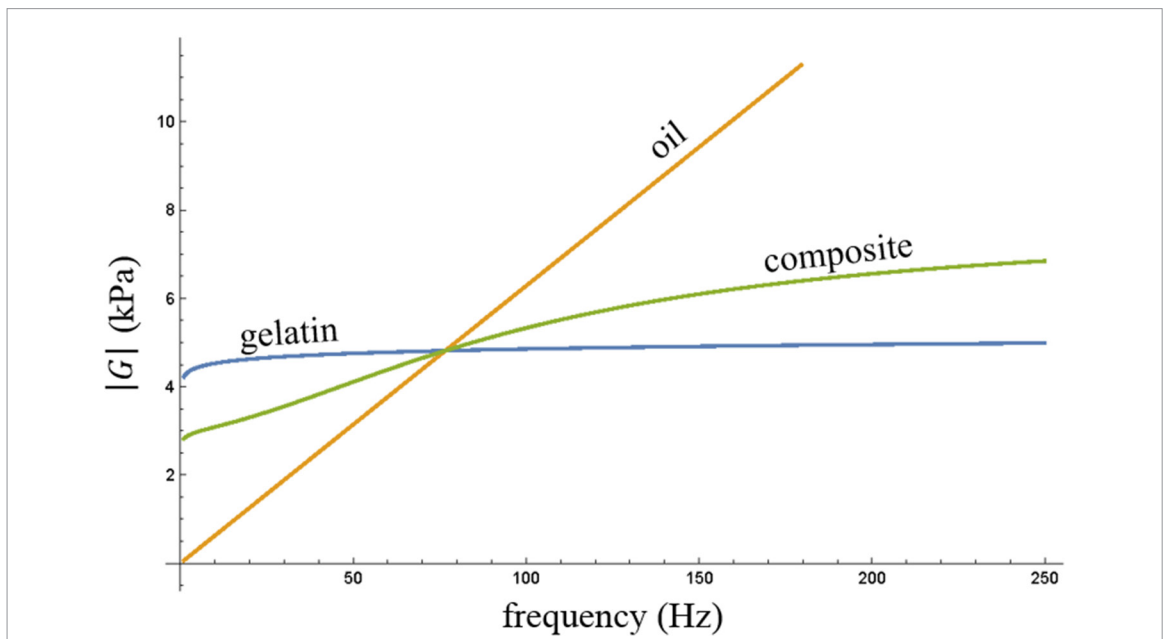


Figure 3. Magnitude of complex shear modulus versus frequency for a power law material such as gelatin, a purely viscous material such as castor oil, and the composite mixture when spherical drops of oil (20% by volume) are suspended in gelatin. As can be noted, the frequency dependence creates different scenarios depending on what range one is examining.

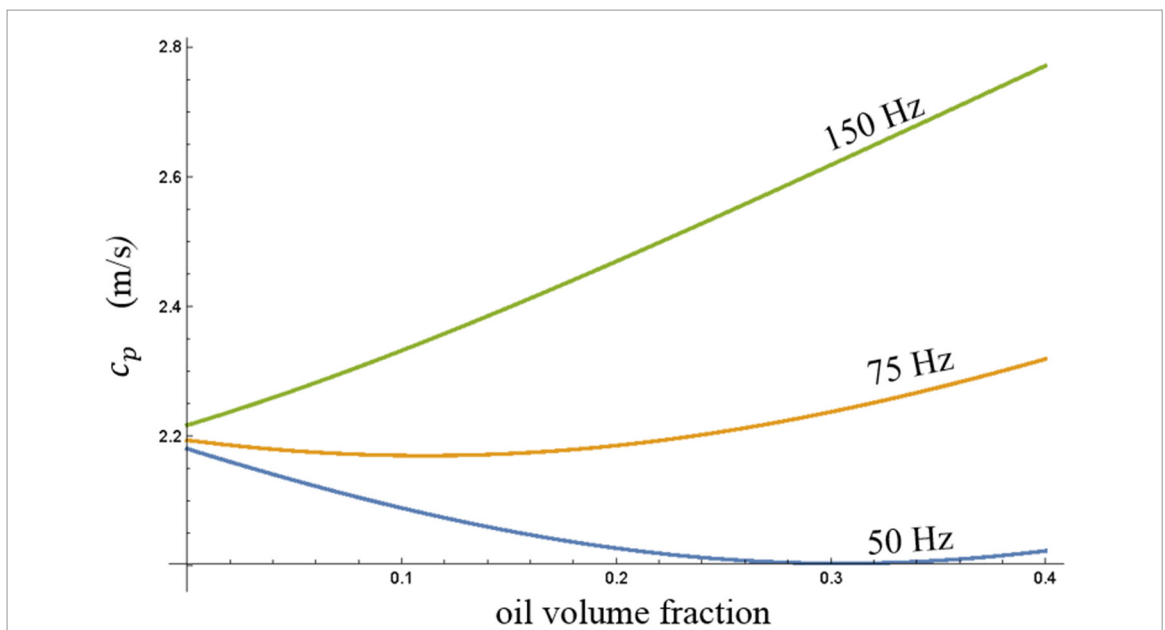


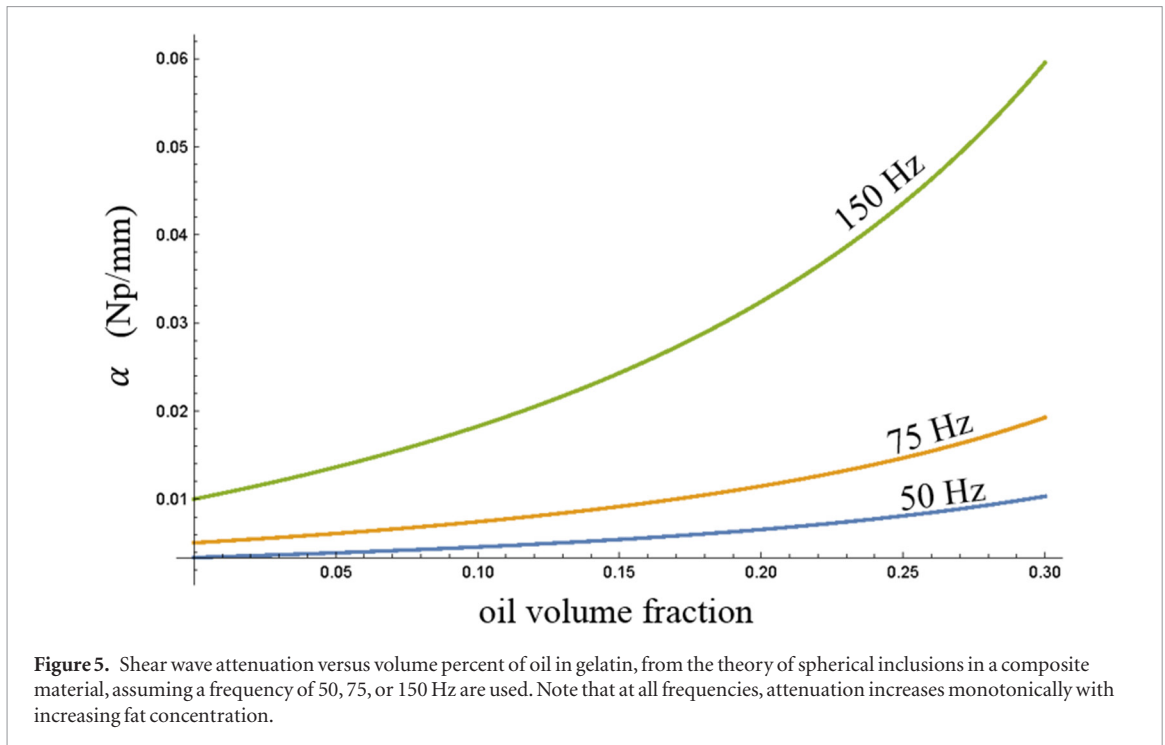
Figure 4. Shear wave speed (phase velocity) versus volume percent of oil in gelatin from the theory of spherical inclusions in a composite material at three different frequencies. Note that conclusions about the effect of increasing fat concentration can strongly depend on choice of frequency. The crossover frequency around 75 Hz in this figure and in figure 5 depends on particular values used: for higher values of liver $|G|$ the crossover frequency will shift to higher frequencies.

where C is a constant obtained from Poiseuille’s Law. Assuming a continuous distribution of vessels and fluid channels from a largest size r_{max} to a smallest size r_{min} leads to:

$$A(\tau) = \frac{A_0}{\tau^b} \begin{cases} \tau_{min} \leq \tau \leq \tau_{max} \\ \text{or} \\ \frac{C}{r_{max}^4} \leq \tau \leq \frac{C}{r_{min}^4} \end{cases}, \tag{6}$$

where b is the power law parameter related to the fractal branching vasculature. Then the resulting stress relaxation function is given by the four parameter microchannel flow model (Parker 2014, 2015, 2017a).

Specifically, the stress relaxation response $\sigma_{SR}(t)$ will be:



$$\sigma_{SR}(t) = \frac{A_0 \left(\Gamma \left[a, \frac{t}{\tau_{\max}} \right] - \Gamma \left[a, \frac{t}{\tau_{\min}} \right] \right)}{t^a}, \quad (7)$$

where Γ is the upper-tailed Gamma function and $a = b - 1$, typically $0 < a \leq 0.5$ in tissues. This model reduces to the two parameter power law (equation (3)) in the limit as $\tau_{\min} \rightarrow 0$ and $\tau_{\max} \rightarrow \infty$, and in that case the parameter a is the same as equation (3). Next, assume that all vessel radii are increased or decreased by some proportion χ , where $\chi = 1$ represents the baseline case and after vessel dilation or constriction:

$$r_2 = \chi r \begin{cases} \chi > 1 \text{ implies dilation} \\ \chi < 1 \text{ implies constriction} \end{cases}. \quad (8)$$

We apply the transformation rule to determine the new stress relaxation spectrum $A_2(\tau_2)$, where $\tau_2 = C/(r_2)^4 = C/(\chi r)^4 = (1/\chi)^4 \tau$, so $d\tau_2/d\tau = (1/\chi)^4$, and find:

$$A_2(\tau_2) = \frac{\chi^4 A_0}{(\tau_2 \chi^4)^b} = \frac{\chi^{4(1-b)} A_0}{\tau_2^b}. \quad (9)$$

Now integrating $\int_{\tau_{2\min}}^{\tau_{2\max}} A_2(\tau_2) e^{-t/\tau_2} d\tau_2$ we find:

$$\sigma_{SR2}(t) = \frac{A_0 \left(\Gamma \left[a, t/\tau_{2\max} \right] - \Gamma \left[a, t/\tau_{2\min} \right] \right)}{\chi^{4a} t^a} \quad (10)$$

where $a = b - 1$, $\tau_{2\max} = \tau_{\max}/\chi^4$, and $\tau_{2\min} = \tau_{\min}/\chi^4$. Thus, equation (10) provides the transformation of elastic properties as a function of vascular diameter changes proportional to χ in some organ.

Although all the terms in equation (10) play a role, for simplicity we focus on the leading term and write

$$\sigma_{SR2}(t) \cong \frac{\sigma_{SR}(t)}{\chi^{4a}}. \quad (11)$$

In other words, if the vessels become constricted, $\chi < 1$ and the second stress relaxation σ_{SR2} is higher (stiffer) than the original $\sigma_{SR}(t)$. Similarly, the liver's complex modulus, originally $G_1(\omega)$ in equation (3), becomes $G_1(\omega)/\chi^{4a}$ in this simplified model. This is indicated in figure 2(c) by the symbol G_1/χ^{4a} as the principal effect of the crowded space on the stiffness of the liver as steatohepatitis progresses. Additional details on the change in function (equation (10)) with χ and its complex modulus are found in section 2 of Parker *et al* (2016).



Figure 6. Two cylindrical phantoms placed in an ice bath, the samples rotated approximately 4 h before they were placed in a refrigerator overnight.

Table 1. Materials used to make seven homogeneous viscoelastic phantoms.

Material	Concentration (%)	Amount	Type
Gelatin	4	33.34 g	300 Bloom Pork Gelatin, Gelatin Innovations Inc., Schiller Park, IL, USA
NaCl	0.9	7.2 g	Sodium Chloride, BDH, West Chester, PA, USA
Agar	0.15	1.2 g	Difco Agar technical, Becton, Dickinson & Comp. Sparks, MD, USA
Castor oil	2, 6, 12, 18, 24, 30, 36	16, 48, 96, 144, 192, 240, 288 ml	Castor oil, Walter Price St. Cayce, SC, USA
Surfactant	30 cc/liter of castor oil	0.48, 1.44, 2.88, 4.32, 5.76, 7.2, 8.64 cc	Ultra-Ivory, Proctor and Gamble Company, Cincinnati, OH, USA

3. Methods

3.1. Homogeneous viscoelastic phantoms

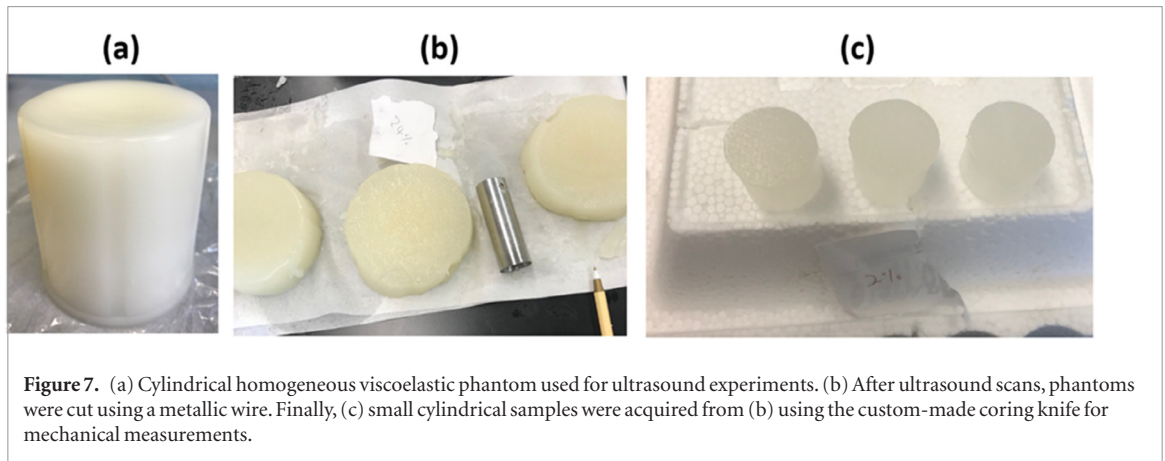
Homogeneous viscoelastic phantoms were constructed as follows. Seven different concentrations of oil-in-gelatin phantoms were created by first heating a mixture of gelatin, degassed water (800 ml), NaCl, and agar to 65 °C. The 65 °C molten gelatin was then mixed with castor oil (also at 65 °C), resulting in seven different percent oil concentrations. A commercially available surfactant was used to facilitate oil droplets that are sufficiently small to remain in suspension during congealing. The solutions were stirred until the mixtures were cooled to about 35 °C. Next, the solutions were poured into cylindrical molds (10 cm diameter \times 10 cm high), placed in an ice bath, and rotated for approximately 4 h in a modified low-speed rotator (model 33B, LORTONE, Inc, Mukilteo, WA, USA) in contact with crushed ice (see figure 6).

Then, the molds were allowed to rest at 4 °C overnight. Table 1 shows the materials in detail and the exact amount for each phantom.

Before subsequent experiments were performed, these phantoms were taken out of the molds and allowed to rest until their temperature was 20 °C. Temperature was confirmed using an infrared thermometer (model 1080, ETEKCITY, Anaheim, CA, USA). All the experiments were performed 1 d later to avoid long-term instability issues with the phantoms.

3.2. Ultrasound measurements

A Samsung ultrasound system (model RS85, Samsung Medison, Seoul, South Korea) and a curved array ultrasound transducer (model CAI-7A, Samsung Medison, Seoul, South Korea) were used to produce radiation force push beams and track the induced displacements. In this experiment, fewer than 100 elements of the transducer were used to transmit focused push beams (center frequency = 2.5 MHz, 130 μ s push duration, multi-focal depth). After push transmission, the Samsung system immediately switched to plane wave imaging mode (center frequency = 3.2 MHz). The sampling frequency rate was set to 20 MHz. Some averaging over depth and noise reduction filtering are applied to the displacement estimates, the fine details are proprietary to Samsung. Shear wave speed and shear wave attenuation coefficients were obtained using the theory reported in Parker and Baddour (2014) and Parker *et al* (2018).



3.3. Mechanical measurements

After the ultrasound scans were completed, three cylindrical samples (approximately 20 mm in diameter \times 17 mm in length) were extracted for each viscoelastic phantom using a custom-made coring knife. Figure 7 shows a viscoelastic phantom used for ultrasound scans and the samples used for mechanical measurements.

For each sample, compression tests were performed using a QT/5 mechanical device (MTS Systems Co., Eden Prairie, MN, USA) with a 5 N load cell to measure the stress/strain and the stress relaxation responses at a sampling rate of 10 Hz. The compression rate and the strain value were adjusted to 0.5 mm s^{-1} and 5%, respectively. These conventional mechanical measurements were considered the reference when assessing the elasticity properties of the cylindrical phantom. Similar to Zhang *et al* (2007) and Ormachea *et al* (2016), the stress relaxation curve of each sample was fitted to the Kelvin–Voigt fractional derivative (KVFD) model using standard non-linear least squares procedures. This viscoelastic model contains three parameters: E_0 , ζ , and a . E_0 refers to the relaxed elastic constant, ζ refers to the viscoelastic parameter, and a refers to the order of fractional derivative. The complex modulus $E^*(\omega)$ is given by

$$E^*(\omega) = \left[E_0 + \zeta \cos\left(\frac{\pi a}{2}\right) \omega^a \right] + j \left[\zeta \sin\left(\frac{\pi a}{2}\right) \omega^a \right]. \quad (12)$$

From our stress relaxation data, the curve fit model parameters E_0 , ζ , and a were then used to predict the shear wave properties near 100 Hz. Note that when $E_0 \approx 0$, the KVFD model reduces to a two-parameter power law equivalent to equation (3).

4. Results

As oil-in-gelatin suspensions increase in volume from 2% to 36%, the general trend is towards decreased stress relaxation force, as shown in figure 8, and increased power law parameter a as the volume percent of oil is increased. At the same time, the baseline shear modulus ζ decreases, indicating a softening at low frequencies, as shown in table 2 (correlation coefficient fitting parameter, R^2 , indicates a good correspondence between the theory model and measurements).

The E_0 parameter is negligible in all cases, consistent with observations in tissues (Zhang *et al* 2007), and consistent with a general two-parameter power law function. The shear wave speed (group velocity) is shown in figure 9 to be decreasing as oil concentration increases. Independent predictions of shear wave speed obtained from the KVFD model using the data in table 2 and the relationship $c_p/\sqrt{G_c(\omega)/\rho}$ from equation (5) using $G_1 = 4 \text{ kPa}$, $\eta = 0.11 \text{ Pa} \cdot \text{s}$, $a = 0.025$, and $\rho = 1000 \text{ kg m}^{-3}$ are also shown at 100 Hz, with reasonable correspondence. 100 Hz is chosen as it represents the approximate spectral peak of the shear wave pulses.

The attenuation estimates are shown to be increasing as a function of oil concentration in figure 10. Independent predictions of attenuation obtained from the KVFD model using the data in table 2 and from the theory model using $G_1 = 4 \text{ kPa}$, $\eta = 0.11 \text{ Pa} \cdot \text{s}$, $a = 0.025$, and $\rho = 1000 \text{ kg m}^{-3}$. For both independent measurements, the complex wave number \hat{k} was calculated and then the imaginary part was obtained using equation (5). Strictly speaking, the composite model results from equation (2) shown in figures 9 and 10 as solid lines are valid only for small volume fractions of oil (Christensen 1969), and are less valid as V approaches 0.5. However, the fit seems reasonable through $V = 0.36$, representing the highest oil concentrations in this study.

5. Discussion

The composite formula explains a number of observations that have appeared in the literature over the last few years. The 70 mouse liver study of Barry *et al* (2014a) found an increase in dispersion of shear wave speed with the

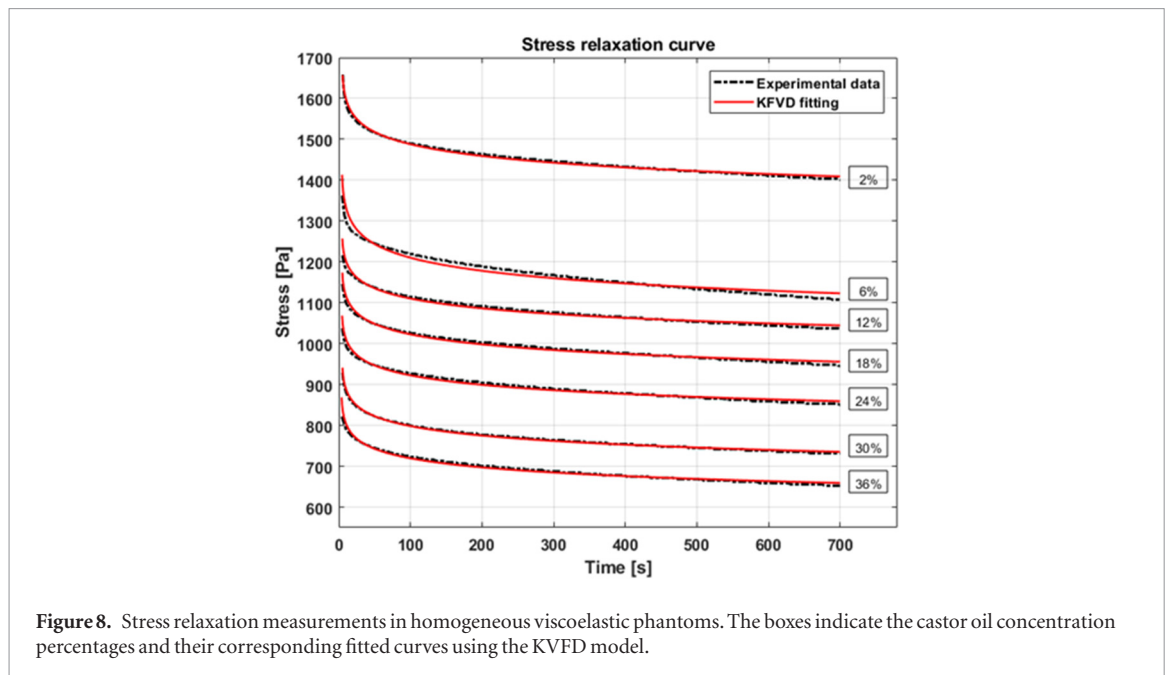
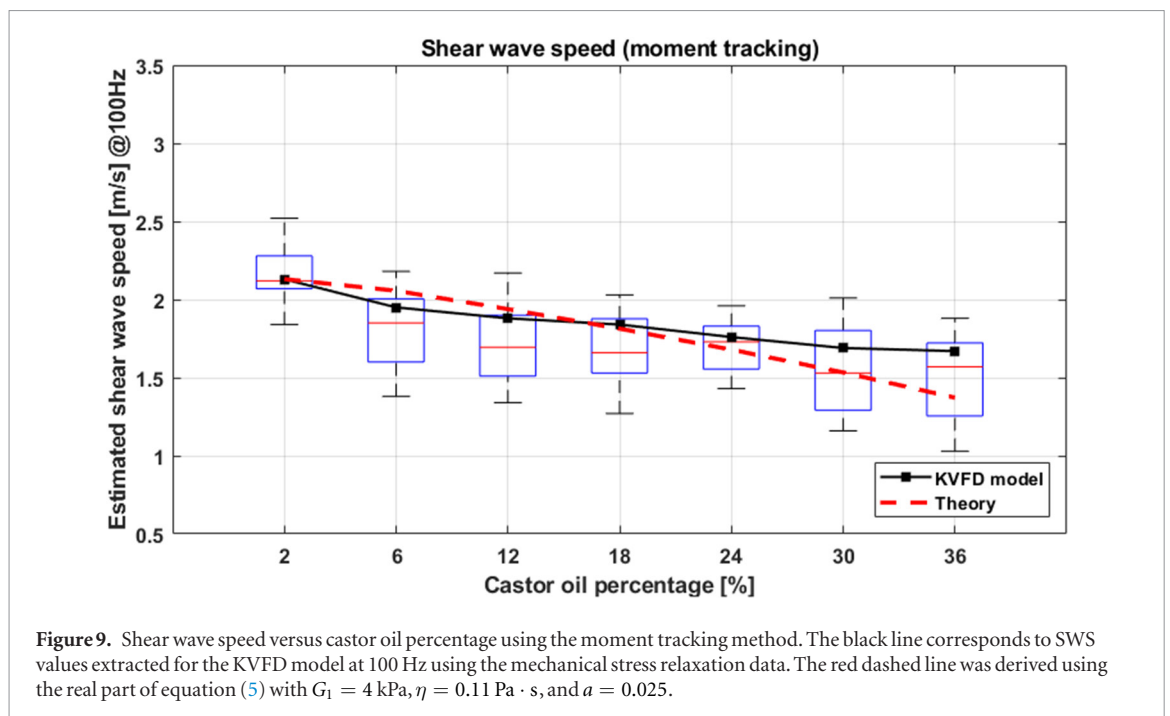
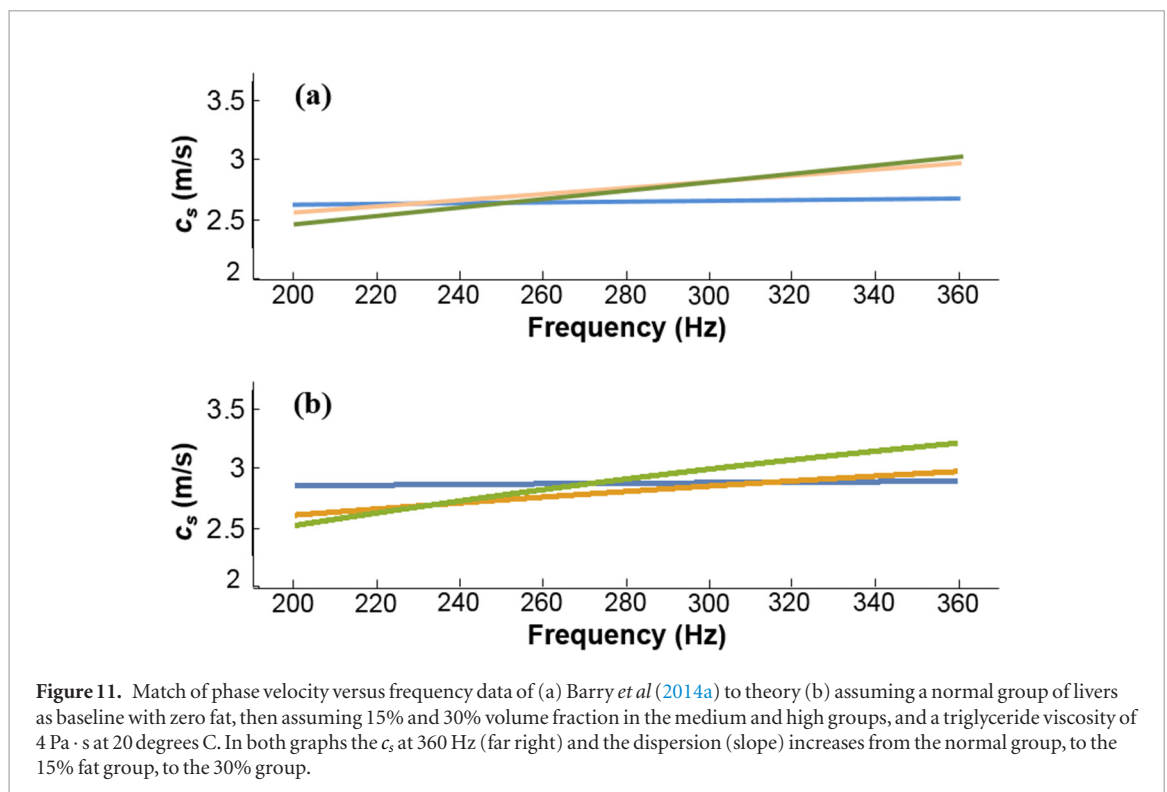
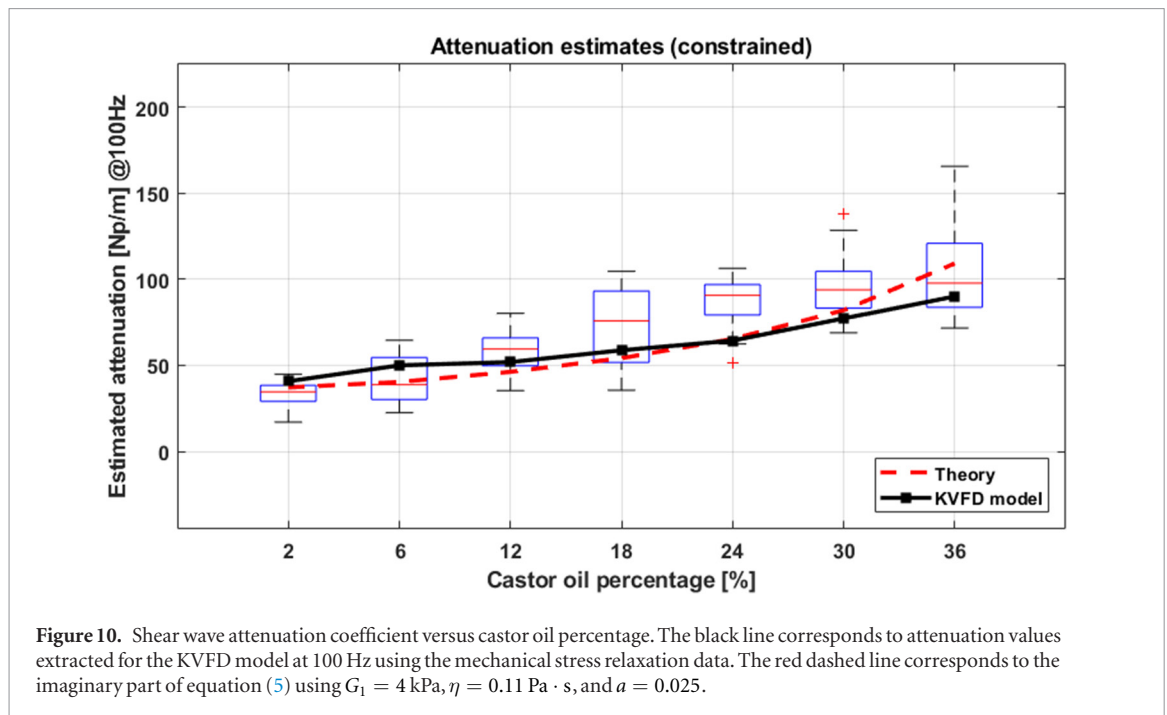


Table 2. Curve fit model parameters using the KVF model for stress relaxation measurements.

Castor oil	E_0 [Pa]	ζ [$\text{Pa} \cdot \text{s}^a$]	a	R^2
2%	0.0016	1.14×10^4	0.0277	0.990
6%	5.02×10^{-4}	9.37×10^3	0.0305	0.964
12%	2.46×10^{-4}	8.64×10^3	0.0311	0.976
18%	8.26×10^{-5}	8.11×10^3	0.0344	0.978
24%	7.95×10^{-5}	7.37×10^3	0.0362	0.976
30%	3.46×10^{-5}	6.57×10^3	0.0417	0.994
36%	1.95×10^{-4}	6.14×10^3	0.0477	0.978



high triglyceride group. Figure 11(a) summarizes the linear fit of phase velocity versus frequency for three groups. Figure 11(b) provides the match using the composite formula, equation (2), with the following parameters: for liver a conventional power law model (equation (3)) is used with $G_1 = 6 \text{ kPa}$ with a power law $a = 0.03$. For the triglycerides in vacuoles, a pure viscosity (equation (4), no stiffness) of $\eta = 4 \text{ Pa} \cdot \text{s}$ is used, and three groups



are shown representing volume fraction of triglyceride as 0, 15%, and 30%. The match of theory and data are reasonable, and the viscosity used in the model ($4 \text{ Pa} \cdot \text{s}$) is higher than that reported for raw Castor oil, but lower than those of more complex fluids such as honey at room temperature (Lide 2005).

Next, the theory can match the rat liver study of Barry *et al* (2015). Figures 12(a) and (b) show the experimental linear curve fit and the composite model match, respectively. Here the measurement frequency range is lower than in the mouse study, and the match is modeled with the liver now at $G_1 = 9 \text{ kPa}$ and the triglyceride in vacuoles having a viscosity of $\eta = 9 \text{ Pa} \cdot \text{s}$, both higher than in the case of the mouse study but some difference is expected given the size, age, diet, and species difference.

Also the theory explains the seemingly divergent measurements of Ogawa *et al* (2016) with respect to steatosis. In their study, the Instron measurements of Young's modulus of excised livers showed a decrease of nearly 50% in stiffness from normal to high steatosis score. However this was contradicted by an 18% increase in shear wave speed measured by a 5 MHz Supersonic imaging system, comparing normals to a group with high steatosis score.

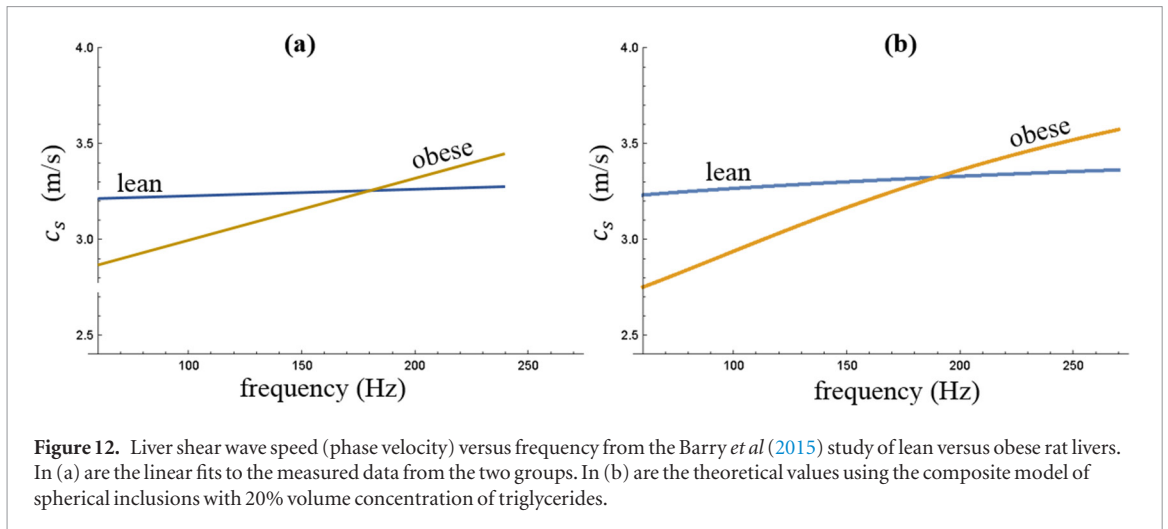


Figure 12. Liver shear wave speed (phase velocity) versus frequency from the Barry *et al* (2015) study of lean versus obese rat livers. In (a) are the linear fits to the measured data from the two groups. In (b) are the theoretical values using the composite model of spherical inclusions with 20% volume concentration of triglycerides.

Given our theoretical models, we note that the Instron measurements correspond to low frequency response, whereas the Supersonic shear wave speed corresponds to group velocity with the peak spectral content likely above 100 Hz. Both observations are consistent with theory as illustrated in figures 3 and 12(b).

For the effect of inflammation, Ogawa *et al* (2016) found an increased stiffness from 6.5 kPa (score 0) to 8.4 kPa (score 3). This corresponds to our theory where $1/x^{4a} = 8.4/6.5$, and assuming $a = 0.24$ (Ormachea *et al* 2016) for liver, then $\chi = 0.77$, implying that the overcrowding of the volume within the liver capsule has reduced vessel diameters by just over 20%, which would have additional hemodynamic effects.

The theories herein can also be compared with more recent results from Kazemirad *et al* (2017), who measured shear wave group velocity in a lower frequency range (40–130 Hz shear wave frequencies) and a higher frequency range (130–220 Hz) in rat livers following the effects of specialized diets. They concluded that liver stiffness decreased with steatosis but increased with inflammation in both frequency bands. These are consistent with the general predictions of our models. However, examining the simple steatosis results, since both frequency bands reported a decrease in stiffness with the 1-week cohort (steatosis grades 2 and 3) this implies the ‘crossover frequency’ depicted in our figures 3, 11 and 12, would lie above 220 Hz for the specific rat livers used in Kazemirad *et al*. That would be consistent with the results of Barry *et al* (2014a) replotted in figure 11, despite the difference in species.

Turning to the issue of models, we note that in section 3.3 we choose a KVFD model as a representative rheological model for gelatin phantoms. However, the addition of viscous oil vacuoles leads to the later modifications. Strictly speaking, the composite model of equation (2) is not guaranteed to exhibit idealized KVFD behavior. Fortunately, the frequency dependence of the viscous component $G_2(\omega)$ creates a composite result that is still relatively compatible with the KVFD behaviors: increasing the power law parameter a and decreasing the stiffness ζ . This can be seen in figure 8 in the time domain and table 2.

We note that other effects and models are possible. Scattering and structural effects have been proposed to explain dispersion (Sack *et al* 2013, Lambert *et al* 2015). These may have an influence. However, scattering of shear waves in a viscoelastic medium is complicated by mode conversion and so a full treatment requires knowledge of a range of parameters of both the medium and the inclusions (Einspruch *et al* 1960). In addition, strong frequency-dependent fluid flow effects are likely in the microchannel flow model above 500 Hz shear waves (Parker 2017b), and these have yet to be considered. Also, the role of the liver capsule and its time constants for expansion require further research.

We have focused on early stage steatosis and steatohepatitis and reserve the biomechanics of high-grade fibrosis for separate consideration. However, considering the clinical studies designed to assess steatosis, a pertinent general observation should be noted. A clinical study designed to assess simple steatosis should avoid enrolling patients with high grade fibrosis. From the view of pathology, the two conditions (simple steatosis versus high grade fibrosis with steatosis) are dramatically different in form and composition. From the viewpoint of biomechanics, high grade fibrosis is associated with $G(\omega)$ that are so elevated as to be off the scale of figure 3, and thus any influence of fat is likely to be ‘camouflaged’ under the dramatic elevation of $G(\omega)$, whatever its particular form. For these reasons, we recommend a partition of elastographic studies of steatosis as logically requiring at least two categories with respect to the presence or absence of significant fibrosis.

6. Conclusion

The biomechanics of simple steatosis and then steatohepatitis are examined using the theory of composite spherical inclusions to model the macrovesicles of fat, and then the microchannel flow model to model

the overcrowded space within the liver capsule in cases where progression to higher grades of steatosis and inflammation have occurred. These theories are shown to explain some of the contradictory results found in the literature, principally due to the strong frequency dependent effects that are present in the biomechanics of steatosis. Careful design of clinical studies and parameter estimations will be required to translate these findings into routine diagnostic assessments using elastography.

Acknowledgments

We are grateful for support from Samsung Medison Co. Ltd and for loan of the equipment. The authors are also thankful for insightful advice from Dr Robert Mattrey, Dr Deborah Rubens, and Professor Kenneth Hoyt about the properties of the liver. We also acknowledge the role of the late Dr Edwin Carstensen, whose persistent questioning of the deepest issues inspired much of the background work.

ORCID iDs

K J Parker  <https://orcid.org/0000-0002-6313-6605>

M G Drage  <https://orcid.org/0000-0003-2593-8268>

References

- Barr R G 2018 Shear wave liver elastography *Abdom. Radiol.* **43** 800–7
- Barr R G *et al* 2015 Elastography assessment of liver fibrosis: society of radiologists in ultrasound consensus conference statement *Radiology* **276** 845–61
- Barry C T, Hah Z, Partin A, Mooney R A, Chuang K H, Augustine A, Almudevar A, Cao W, Rubens D J and Parker K J 2014a Mouse liver dispersion for the diagnosis of early-stage Fatty liver disease: a 70-sample study *Ultrasound Med. Biol.* **40** 704–13
- Barry C T, Hazard C, Hah Z, Cheng G, Partin A, Mooney R A, Chuang K H, Cao W, Rubens D J and Parker K J 2015 Shear wave dispersion in lean versus steatotic rat livers *J. Ultrasound Med.* **34** 1123–9
- Blackstock D T 2000 *Fundamentals of Physical Acoustics* (New York: Wiley)
- Carstensen E L and Parker K J 2014 Physical models of tissue in shear fields *Ultrasound Med. Biol.* **40** 655–74
- Christensen R M 1969 Viscoelastic properties of heterogeneous media *J. Mech. Phys. Solids* **17** 23–41
- Cosgrove D *et al* and (EFSUMB) 2013 EFSUMB guidelines and recommendations on the clinical use of ultrasound elastography. Part 2: clinical applications *Ultraschall Med.* **34** 238–53
- Einspruch N G, Witterholt E J and Truell R 1960 Scattering of a plane transverse wave by a spherical obstacle in an elastic phantom *J. Appl. Phys.* **31** 806–18
- Hessheimer A J, Parramon D, Guimera A, Erill I, Rimola A, Garcia-Valdecasas J C, Villa R and Fondevila C 2009 A rapid and reliable means of assessing hepatic steatosis *in vivo* via electrical bioimpedance *Transplantation* **88** 716–22
- Kazemirad S, Zhang E, Nguyen B N, Bodson-Clermont P, Destremes F, Trudel D, Cloutier G and Tang A 2017 Detection of steatohepatitis in a rat model by using spectroscopic shear-wave US elastography *Radiology* **282** 726–33
- Lakes R S 2009 *Viscoelastic Materials* (Cambridge: Cambridge University Press) ch 9
- Lambert S A, Nasholm S P, Nordsletten D, Michler C, Juge L, Serfaty J M, Bilston L, Guzina B, Holm S and Sinkus R 2015 Bridging three orders of magnitude: multiple scattered waves sense fractal microscopic structures via dispersion *Phys. Rev. Lett.* **115** 094301
- Lide D R 2005 *CRC Handbook of Chemistry and Physics: 2005–2006: a Ready-Reference Book of Chemical and Physical Data* (Boca Raton, FL: CRC Press)
- Ogawa S, Moriyasu F, Yoshida K, Oshiro H, Kojima M, Sano T, Furuichi Y, Kobayashi Y, Nakamura I and Sugimoto K 2016 Relationship between liver tissue stiffness and histopathological findings analyzed by shear wave elastography and compression testing in rats with non-alcoholic steatohepatitis *J. Med. Ultrason* **43** 355–60
- Ormachea J, Lavarello R J, McAleavey S A, Parker K J and Castaneda B 2016 Shear wave speed measurements using crawling wave sonoelastography and single tracking location shear wave elasticity imaging for tissue characterization *IEEE Trans. Ultrason. Ferroelectr. Freq. Control* **63** 1351–60
- Parker K J 2014 A microchannel flow model for soft tissue elasticity *Phys. Med. Biol.* **59** 4443–57
- Parker K J 2015 Experimental evaluations of the microchannel flow model *Phys. Med. Biol.* **60** 4227–42
- Parker K J 2017a Are rapid changes in brain elasticity possible? *Phys. Med. Biol.* **62** 7425–39
- Parker K J 2017b The microchannel flow model under shear stress and higher frequencies *Phys. Med. Biol.* **62** N161–7
- Parker K J and Baddour N 2014 The Gaussian shear wave in a dispersive medium *Ultrasound Med. Biol.* **40** 675–84
- Parker K J, Ormachea J, McAleavey S A, Wood R W, Carroll-Nellenback J J and Miller R K 2016 Shear wave dispersion behaviors of soft, vascularized tissues from the microchannel flow model *Phys. Med. Biol.* **61** 4890–903
- Parker K J, Ormachea J, Will S and Hah Z 2018 Analysis of transient shear wave in lossy media *Ultrasound Med. Biol.* accepted (<https://doi.org/10.1016/j.ultrasmedbio.2018.03.014>)
- Sack I, Johrens K, Wurfel J and Braun J 2013 Structure-sensitive elastography: on the viscoelastic powerlaw behavior of *in vivo* human tissue in health and disease *Soft Matter* **9** 5672–80
- Selzner M and Clavien P A 2001 Fatty liver in liver transplantation and surgery *Semin. Liver Dis.* **21** 105–13
- Srinivasa Babu A, Wells M L, Teytelboym O M, Mackey J E, Miller F H, Yeh B M, Ehman R L and Venkatesh S K 2016 Elastography in chronic liver disease: modalities, techniques, limitations, and future directions *Radiographics* **36** 1987–2006
- Wada K, Fujimoto K, Fujikawa Y, Shibayama Y, Mitsui H and Nakata K 1974 Sinusoidal stenosis as the cause of portal hypertension in choline deficient diet induced fatty cirrhosis of the rat liver *Acta Pathol. Japan* **24** 207–17
- Watson R R 1991 *Liver Pathology and Alcohol* (Totowa, NJ: Humana Press)
- Zhang M, Castaneda B, Wu Z, Nigwekar P, Joseph J V, Rubens D J and Parker K J 2007 Congruence of imaging estimators and mechanical measurements of viscoelastic properties of soft tissues *Ultrasound Med. Biol.* **33** 1617–31